



Fabrication of hollow mesoporous $\text{SiO}_2\text{-BiOCl@PANI@Pd}$ photocatalysts to improve the photocatalytic performance under visible light

Yi Tian, Wei Li, Chenhui Zhao, Yufei Wang, Baoliang Zhang, Qiuyu Zhang*

Department of Applied Chemistry, School of Natural and Applied Sciences, Northwestern Polytechnical University, Xi'an 710072, China

ARTICLE INFO

Article history:

Received 18 February 2017

Received in revised form 2 May 2017

Accepted 7 May 2017

Available online 9 May 2017

Keywords:

Hollow mesoporous silica

Hybrid photocatalysts

LSPR

BiOCl

Polyaniline

ABSTRACT

A facile method was developed to synthesize a series of hollow mesoporous $\text{SiO}_2\text{-BiOCl@PANI@Pd}$ (HBPP) photocatalysts with super adsorption performance, plasmonic effect and fast interfacial charge migration. The samples were characterized by XRD, FETEM, FT-IR, XPS, DRS, etc. Photocatalytic degradation of methyl orange (MO) by HBPP composites was investigated.

Results showed that the photocatalytic property of HBPP composite was superior to that of hollow mesoporous $\text{SiO}_2\text{-BiOCl@PANI}$ (HBP) composite under visible light irradiation, and the HBPP_{5wt%} photocatalyst synthesized under 140 °C exhibits the highest photocatalytic activity. In this photocatalysis system, the orderly mesoporous opening structure of the hollow mesoporous SiO_2 sphere could effectively facilitate the transfer of reactant molecules, and the existence of the internal cavities would effectively prolong the action time of the irradiated light for the multiple reflections. Moreover, the formation of interacted interfaces between the semiconductor BiOCl and conducting polymer (polyaniline) could effectively improve the separation of the photogenerated electron-hole pairs, and the palladium nanoparticles (Pd NPs) with strong localized surface plasmon resonance (LSPR) absorption band in the near-UV region could effectively induce the generation of the photoexcited electron-hole pairs in BiOCl , thus the as-obtained photocatalyst exhibits superior photocatalytic activity under visible light irradiation. The work may set foundation for application of the new photocatalyst of HBPP-based LSPR and make an important step forward remedying environmental pollution.

© 2017 Published by Elsevier B.V.

1. Introduction

As a promising material, photocatalysts have attracted considerable attention in applications of remedying environmental pollution and dealing with energy crisis [1–5]. During the last two decades, the most widely TiO_2 has been developed in pursuit of high photocatalytic activity, high chemical stability, relative low-price and nontoxicity. However, the wide band gap (3.2 eV) and low quantum yield of TiO_2 limit its application in visible light range. Therefore, the work focused on TiO_2 modifications and the pursuit of better photocatalysts have attracted more attention in recent years. It's known that photocatalysis system can be generally classified as oxides (TiO_2 , ZnO , NiO) [6–8], sulfides (CdS , ZnS) [9,10], and halides (AgCl , AgBr) [11–13], etc. Recently, lamellar BiOX ($X = \text{Cl}$, Br , I) as other species of bismuth-based materials have become a hotspot in photocatalysis field [14–17] for their unique prop-

erties of high dipole, indirect band gaps, high redox potential of holes and easily formed oxygen vacancies. However, some modification approaches to BiOCl semiconductor photocatalysts should be proposed to improve their photocatalytic property for their low visible-light response and low utilization efficiency of photon-generated carriers [3,18–20]. For instance, Yu et al. [21] developed a facile approach to synthesize the highly efficient $\text{Bi}_2\text{O}_2\text{CO}_3/\text{BiOCl}$ photocatalyst. Di et al. [19] synthesized carbon quantum dots (CQDs) modified BiOCl ultrathin nanosheets photocatalyst via a facile solvothermal method. However, in previous studies, the electron was not excited from the valance band to the conductor band in the photocatalytic process of BiOCl .

In recent years, the applications of conducting polymer in photocatalysis field have been reported by many researchers [22–24]. It was demonstrated that introducing conducting polymer is an effective method to improve the photocatalytic performance of traditional semiconductor photocatalyst [25]. Polyaniline (PANI), a recognized promising conducting polymer, has attracted more and more attentions for the $\pi-\pi$ conjugated electronic system, high absorption coefficients under visible light, high charge migra-

* Corresponding author.

E-mail address: qy়zhang@nwpu.edu.cn (Q. Zhang).

tion and good environmental stability [26–28]. Zhang et al. [29] prepared TiO₂ photocatalysts modified with monolayer dispersed PANI via a facile chemisorption approach. Pei et al. [30] prepared PANI hybrid defective ZnO nanoparticles by a facile chemisorption method together with a cold plasma treatment technique. In these photocatalysis systems, the PANI acted as electron donor or hole acceptor to enhance the photocatalytic property under visible light irradiation.

Among numerous modification methods, the introduction of plasmonic nanoparticles (NPs) to traditional photocatalysis system has been extensively studied since it was firstly reported in 2008 [31]. On the one hand, plasmonic nanoparticles can accelerate the process of photoexcited electron transferring to the substrate [13,32–35]. On the other hand, its strong interaction with electromagnetic fields also causes the localized surface plasmon resonance (LSPR) in the near-UV region, which is demonstrated to boost the excitation of electron-hole pairs in wide band semiconductor (i.e. TiO₂) and increase photocatalytic efficiency. Kowalska et al. [36] prepared hybrid photocatalysts composed of titania modified with plasmonic nanoparticles and ruthenium complexes for decomposition of organic compounds. Andreas et al. [35] reported a perfect palladium-based plasmonic perfect absorber at visible wavelengths and its application of hydrogen sensing. Moreover, it has not been reported that the palladium-based plasmonic renounce effect excites the electron-hole pairs in semiconductor. In this regard, we have proposed hybrid photocatalysts composed of plasmonic Pd NPs, BiOCl and PANI, as potential efficient materials for decomposition of organic compounds under solar radiation.

To the best of our knowledge, hollow mesoporous silica sub-microspheres (H-mSiO₂), which can fulfill the multiple scattering of the irradiated light in the internal cavity, can efficiently prolong the action time of the irradiated light and promote the generation of the photoexcited electrons. Simultaneously, the orderly mesoporous opening structure can facilitate the transfer of reactant molecules [37–39]. Based on aforementioned consideration, a novel visible-light-driven (VLD) HBPP photocatalyst was successfully synthesized by loading the nanosheet BiOCl semiconductor, PANI conducting polymer and Pd plasmonic nanoparticles on the surface of amino-functionalized H-mSiO₂. Subsequently, MO was chosen as the target organic pollutant, and the photocatalytic activity of the HBPP photocatalyst for degrading MO in water system under the visible light irradiation was investigated, and the possible photocatalytic mechanism was also discussed.

2. Experimental section

2.1. Reagents and materials

All of the reagents were analytical pure. Absolute ethanol (EtOH), ammonia solution (25 wt%), tetraethoxysilane (TEOS), cetyltrimethylammonium bromide (CTAB), anhydrous sodium carbonate (Na₂CO₃), ammonium nitrate (NH₄NO₃), bismuth nitrate pentahydrate (Bi(NO₃)₃·5H₂O), 3-triethoxysilylpropylamine (APTES), potassium chloride (KCl), methyle orange (MO), aniline, Pd(OAc)₂, hydrochloric acid(HCl, 1 mol/L), Ammonium persulfate (APS), polyvinyl pyrrolidone (PVP), potassium iodide (KI), isopropyl alcohol (IPA), *p*-benzoquinone (BQ), AgNO₃ and P25 were purchased from J & K Chemical. Deionized water was used throughout the work.

2.2. The preparation of HBPP

2.2.1. Preparation of amino-functionalized H-mSiO₂

The preparation process was obtained by modifying a reported method [38] (Supplementary Note 1). The solid silica sub-

microspheres were prepared by traditional Stöber hydrolysis method. Subsequently, in the presence of CTAB, the core-shell silica sub-microspheres were prepared by coating the silica on the surface of solid silica sub-microspheres. Moreover, the hollow silica sub-microspheres were prepared by the selective alkaline-tailored method under the protection of CTAB. After that, the mesoporous structure was prepared by calcination at 500 °C. Finally, aforementioned H-mSiO₂ was modified by the APTES at an acetonics system containing a small amount of ammonia solution (25 wt.%).

2.2.2. Preparation of H-mSiO₂-BiOCl@PANI@Pd photocatalyst

The Bi³⁺ ions and Pd²⁺ were anchored on the surface of amino-functionalized H-mSiO₂ under the complexation, and they transform into BiOBr nanosheet and Pd NPs on the surface of H-mSiO₂ by the hydrothermal synthesis. 0.3 g PVP, 0.3 g amino-functionalized H-mSiO₂, 0.5 g Bi(NO₃)₃·5H₂O and 0.025 g Pd(OAc)₂ were sonicated in 300 mL water for 10 min, and stirred for 1 h. In this stirring system, HCl was added to adjust the pH of solution, and 0.5 mL aniline was dissolved in the as-obtained solution. After blending uniformly, 0.01 g/mL 60 mL APS was dissolved in this system until the temperature rising to 40 °C, and the as-obtained mixed system was stirring slowly at 40 °C for 8 h. After the reaction finished, the sample was separated by centrifugalization at the speed of 10000 rpm and washed 2–3 times with distilled water. Subsequently, aforementioned sample was redispersed into 80 mL deionized water containing 0.3 g KCl. Then the mixture in the teflon liner was sealed in a stainless steel autoclave and maintained at 140 °C for 3 h. After cooled naturally to ambient temperature, the resultant products were washed several times with water and ethanol then dried for 12 h via the vacuum freeze-drying technology. To study the effect of the weight percent of Pd (Pd: BiOCl) on the photocatalytic performance of the products, HBPP photocatalysts with different weight percent of Pd (10 wt.%, 7 wt.%, 3 wt.%, 2 wt.% and 0 wt.%) were synthesized via the similar process.

2.3. Characterization

Fourier transform-infrared (FT-IR) spectra of the samples was recorded on a Perkin-Elmer 580BIR spectrophotometer using the KBr pellet technique. X-ray powder diffraction (XRD) analysis was performed on a Bruker AXS D8-advance X-ray diffractometer with Cu Kα radiation. The morphologies and sizes of the samples were characterized using a JEOL JEM-2100F field emission transmission electron microscopy (FETEM). X-ray photoelectron spectroscopy (XPS) data were collected to examine the chemical states of the multi-component photocatalyst with an Axis Ultra instrument (Kratos Analytical, Manchester, U.K.) under ultrahigh vacuum condition (<10⁻⁶ Pa) and using a monochromatic Al Kα X-ray source (1486.6 eV). N₂ adsorption/desorption isotherms were obtained on a TriStar II 20 apparatus. The Brunauer-Emmett-Teller (BET) method was used to calculate the specific surface area based on the adsorption branches. UV-vis diffuse reflectance spectra (DRS) was obtained using a Shimadzu UV-3600 spectrometer by using BaSO₄ as a reference at room temperature.

2.4. Evaluation of photocatalytic properties

The photocatalytic activities of the as-prepared HBPP photocatalyst were evaluated respectively by catalyzing the photodegradation of MO in aqueous solution at room temperature under the visible light irradiation with one 500 W xenon lamp (CHF-XM500, light intensity = 600 mW/cm²) located at 20 cm away from the reaction solution. To make sure that the photocatalytic reaction was really driven by visible-light, all the UV lights with the wavelength less than 420 nm were removed by a glass filter (JB-420). In a typical reaction, 0.1 g of as-prepared supported photocatalyst was

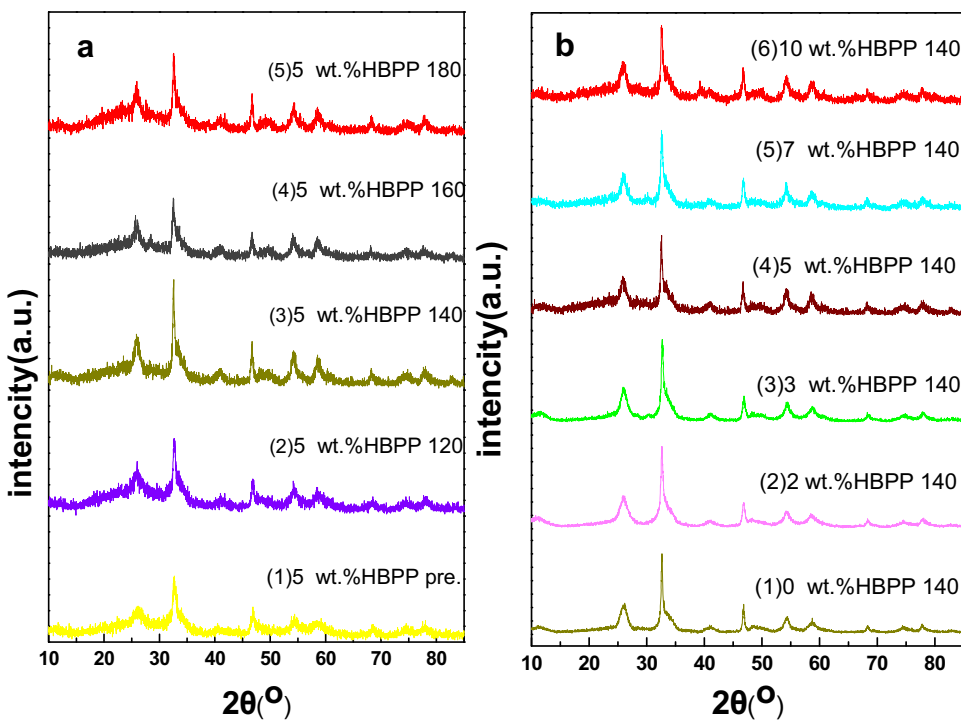


Fig. 1. XRD patterns of as-prepared HBPP synthesized at different conditions.

(a) HBPP_{5wt.%} synthesized at different temperature: ((1) not hydrothermal (2) 120 °C, (3) 140 °C, (4) 160 °C (5) 180 °C); and HBPP synthesized at 140 °C with the different weight percent of Pd((1) 0 wt.%, (2) 2 wt.%, (3) 3 wt.%, (4) 5 wt.%, (5) 7 wt.%, (6) 10 wt.%) for 3 h.

dispersed into 100 mL of dye aqueous solution (50 mg/L). Before light irradiating, the suspension was stirred for 1 h in the dark to reach adsorption equilibrium of dye molecules on the surface of the photocatalyst. Then, 5 mL of reaction solution was extracted at a certain interval during the experiment and centrifuged to remove the powders, and the filtrates are analyzed in aqueous solution by UV-vis spectroscopy to determine the concentration of the dye. The Electron Paramagnetic Resonance (EPR) spectra were conducted on a Bruker model ESR JES-FA200 spectrometer. In this study, the as-prepared HBPP with the different weight percent of Pd was evaluated by the above-mentioned processes.

After experiment finished, the catalyst was collected by centrifugal separation and respectively washed several times with ethanol and distilled water, then the recovered catalyst would undergo the above-mentioned process to evaluate the stability of the HBPP.

2.5. Radical trapping experiments

For detecting the active species during photocatalytic reactivity, hydroxyl radicals ($\cdot\text{OH}$), superoxide radical ($\cdot\text{O}_2^-$), electron (e^-) and holes (h^+) were investigated by adding 2 mg IPA (a scavenger of $\cdot\text{OH}$) [19], 2 mg BQ (a scavenger of $\cdot\text{O}_2^-$) [21], 2 mg AgNO_3 (a scavenger of e^-) and 2 mg KI (a scavenger of h^+), respectively. The method was similar to the former photocatalytic property test.

3. Result and discussion

3.1. Morphology and optical properties of the samples

The phase and crystallographic structure of as-prepared HBPP composites were determined by XRD. Fig. 1a shows the XRD patterns of 5 wt.% HBPP at different hydrothermal temperatures (0–180 °C). The specific diffraction peaks of XRD patterns belong

to the standard values of BiOCl (JCPDS card No. 06-0249) and Pd (JCPDS card No. 65-2867), respectively. Comparing the samples before and after hydrothermal treatment, we find that the diffraction peaks of the former are wider and part of them disappears, for instance, the peak at 2θ value of 49.3° belonging to (113). With the hydrothermal temperature increasing to 120 °C, the diffraction peaks of BiOCl mainly appear. As the hydrothermal temperature further increases to 140 °C, it shows stronger and narrower XRD peaks, which indicates the higher crystallinity. The main diffraction peak corresponding to the (101), (110), (102), (200), (211) and (212) crystal faces of BiOCl appear at 27.8°, 32.4°, 33.4°, 46.2°, 54.1° and 55.7°, respectively. Moreover, the diffraction peak intensity of the (001) plane is the strongest, indicating that BiOCl favors growth along with the (110) facet. Furthermore, as the hydrothermal temperature increases to 160 °C and 180 °C, It is revealed that there are no extra peaks appear and the highest crystallinity of the HBPP_{5wt.%} composite is synthesized at 140 °C.

Fig. 1b shows XRD patterns of HBPP with different weight percent of Pd synthesized hydrothermally at 140 °C for 3 h. As shown in Fig. 1b, the XRD pattern of the Pd NPs partly overlaps with that of the BiOCl, for instance, the peak at 2θ value of 46.6°, 68.4°, 82.7° which correspond to the (200), (220), (311) crystal faces of Pd. Otherwise, as weight percent of Pd increases to 7 wt.%, the diffraction peak position at 40.1° which belongs to the (111) crystal faces of Pd NPs appears a little blue shift while the (112) crystal face of BiOCl at 40.8° has a little red shift, which may be ascribed to an unavoidable lattice distortion that has happened at other situations[18] and also imply the interaction between BiOCl and Pd. Nevertheless, while the weight percent of Pd is lower than 5 wt.%, the diffraction peak of the (111) crystal faces of Pd is un conspicuous, which may indicate that the Pd is possibly dispersed uniformly onto the surface of BiOCl nanobelt.

Fig. 2 shows the TEM, HRTEM images of as-prepared 5 wt.%HBPP samples. As shown in Fig. 2a, the surface of HBPP synthesized before

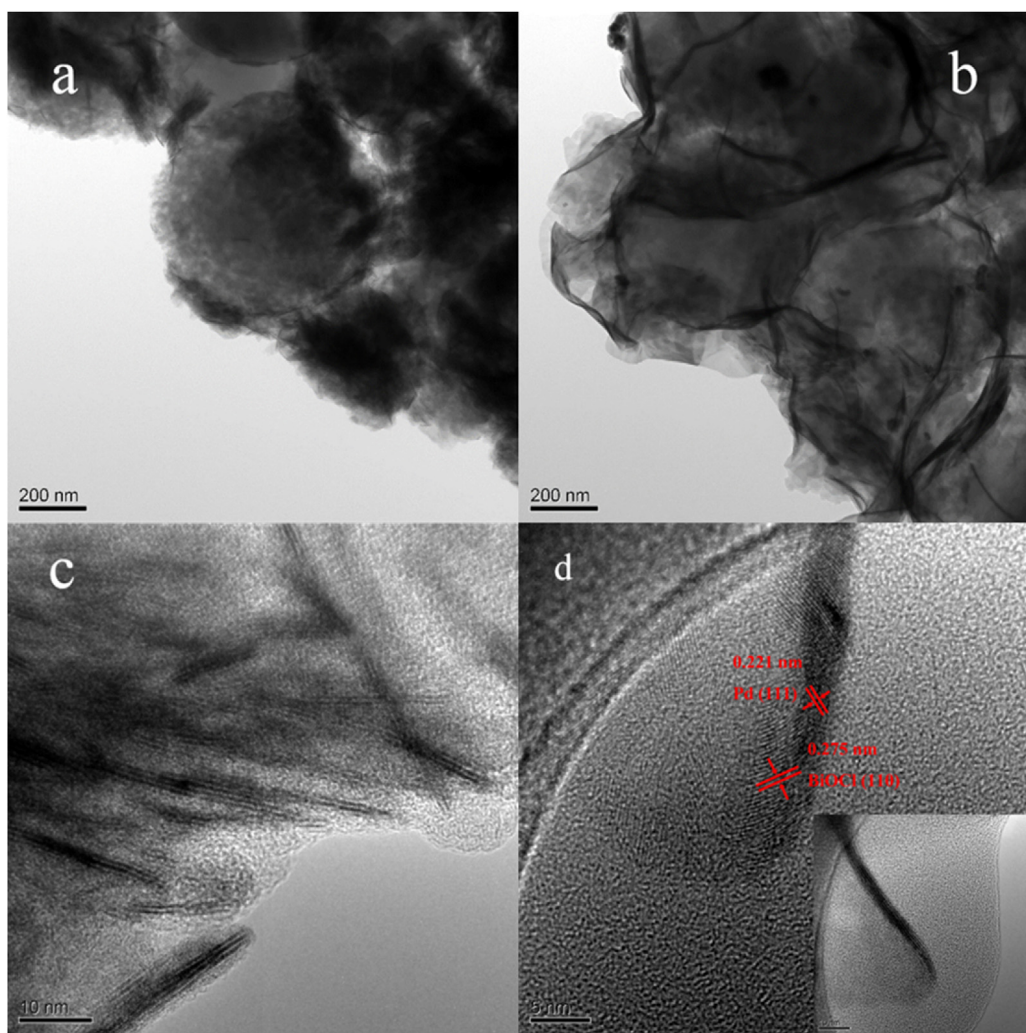


Fig. 2. TEM and HRTEM images of the HBPP_{5wt.%} without hydrothermal process (a, c) and synthesized at 140 °C (b, d).

hydrothermal process is loose. When synthesize at 140 °C for 3 h, it is observed that the BiOCl@PANI@Pd is tightly attached on the surface of hollow mesoporous silica sub-microspheres, indicating the formation of the BiOCl nanosheet. In addition, the particle diameter, as determined from the TEM images (Fig. 2a and b), is found to be decreasing approximately 11% after hydrothermal process for the effect of high temperature and pressure.

Moreover, the nanocrystalline nature of the as-prepared HBPP was characterized by high-resolution transmission electron microscopy (HRTEM). The fringes are obscure in the HRTEM image of HBPP_{5wt.%} before hydrothermal process (as shown in Fig. 2c). Otherwise, the clear BiOCl nanobelt can be seen on the surface of hollow mesoporous silica sub-microspheres when the HBPP_{5wt.%} photocatalyst synthesized at 140 °C (insert of Fig. 2d), and the fringes appearing in the micrograph allow the identification of the crystallographic spacing of BiOCl and Pd in the enlarged view (Fig. 2d). The fringe of $d=0.275\text{ nm}$ matches the (110) crystallographic plane of BiOCl, while the fringe of $d=0.221\text{ nm}$ matches the (111) crystallographic plane of Pd NPs uniformly dispersed on the BiOCl nanobelt and PANI coating. Thus, the clear lattice fringes, a typical characteristic of high crystallinity, and composites structure probably result in high photocatalytic activity of as-prepared photocatalyst.

Fig. 3 shows the FT-IR spectra of hollow mesoporous silica microspheres, as-prepared 5 wt.% HBPP before hydrothermal process and as-prepared 5 wt.% HBPP synthesized at 140 °C for 3 h.

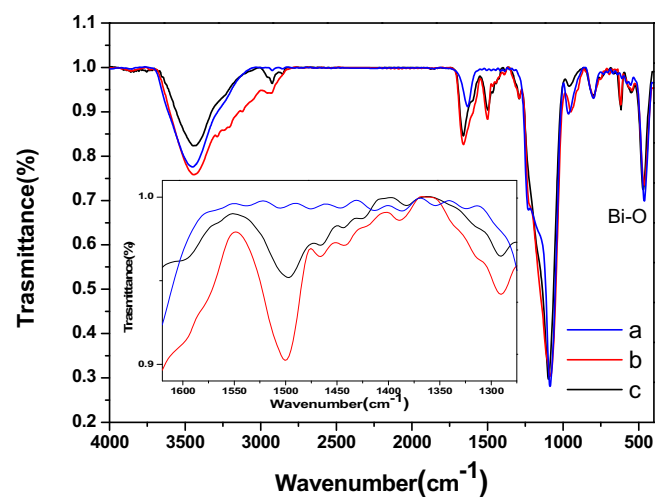


Fig. 3. FT-IR spectrum of (a) H-mSiO₂; (b) 5 wt.% HBPP not hydrothermal; (c) 5 wt.% HBPP prepared at 140 °C for 3 h.

The strong peaks around 600 cm^{-1} were attributed to the Bi—O vibration. Moreover, it is clearly seen that the main characteristic peaks of the hydrothermal HBPP are 1596 cm^{-1} , 1496 cm^{-1} and 1289 cm^{-1} can be attributed to C=N stretching mode for

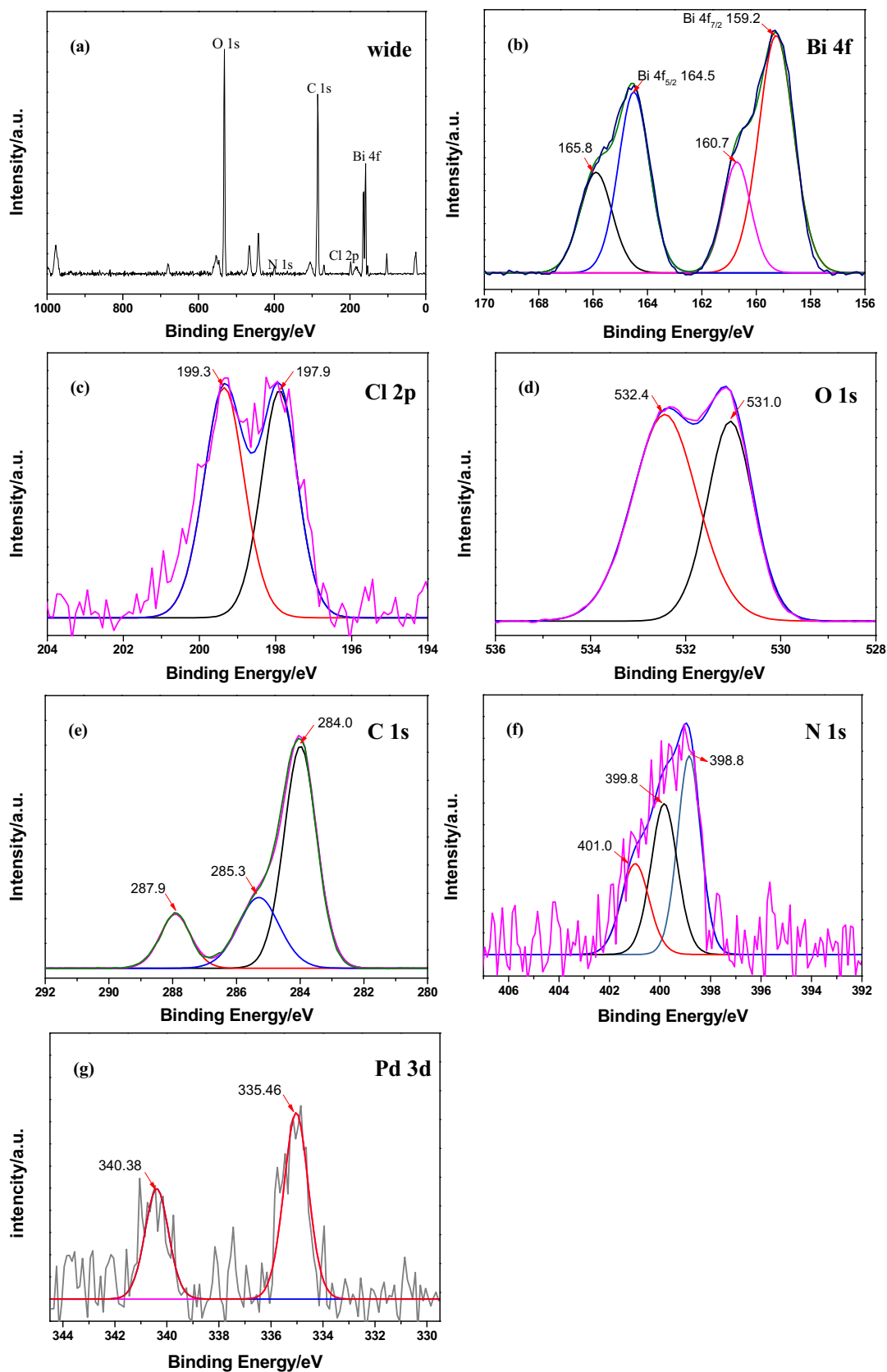


Fig. 4. XPS spectra of the as-prepared HBPP.

the quinonoid unit, C=C stretching mode for the benzenoid unit, and C=N stretching mode of benzenoid unit, respectively, which demonstrates the existence of PANI in the hydrothermal HBPP.

Besides, compared the FT-IR spectras of HBPP before and after hydrothermal process, no extra spectra were found, which means

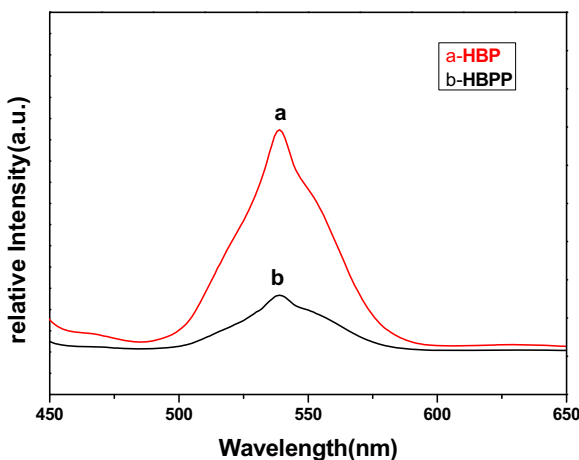


Fig. 5. Photoluminescence spectra of (a) HBP (b) the 5 wt.% HBPP synthesized at 140 °C (excitation at 420 nm at room temperature).

the hydrothermal process in 140 °C has no effect on the structure of PANI.

To investigate the surface compositions and chemical state of the as-prepared HBPP, XPS was carried out and the results of XPS spectra are shown in Fig. 4. It reveals that the surface of this supported photocatalyst is consisted of O, Bi, Cl, C, N and Pd (Fig. 4a).

The Bi 4f spectrum and the corresponding fitting peaks are showed in Fig. 4b. The core lines fixes at 159.2 eV and 164.5 eV are indexed to Bi 4f_{7/2} and Bi 4f_{5/2}, respectively, indicating the existence of Bi³⁺ in BiOCl. Moreover, two small peaks fixed at 160.7 eV and 165.8 eV should be caused by the complexation between Bi atoms and amino-groups on the surface of the hollow mesoporous silica sub-microspheres. Besides, the Cl 2p peaks (Fig. 4c) are associated with the binding energy at 199.3 eV and 197.9 eV. Moreover, Fig. 4d is the O 1s high resolution spectrum, and the peak located at 531.0 eV and 532.4 eV can be ascribed to the BiOCl, and SiO₂.

In addition, the C 1 s core level spectrum of the HBPP sample is quite asymmetric, indicating rich valent states of C atoms (Fig. 4e). The spectral curve can be well fitted into three peaks located at 287.9 eV, 285.3 eV and 284.0 eV, respectively. The peak with the smallest binding energy (BE) is attributed to C atoms only bound to C or H atoms. The peak located at 285.3 eV can be ascribed to C in C—N groups whereas the 287.9 eV centered peak is related to C within C=N species. Fig. 4f shows the XPS spectrum of N 1s in backbone of PANI. The peaks located at 398.9 eV, 399.8 eV, 401.0 eV

corresponds to —N=, —NH—, —NH⁺, respectively, indicating the existence of PANI doping with protonic acid (H⁺). The binding energy of Pd 3d_{3/2} and Pd 3d_{5/2} are ~340.38 eV and ~335.1 eV, respectively, indicating that most Pd component is in the form of metallic Pd nanoparticles. In conclusion, it well demonstrates that the BiOCl@PANI@Pd composite had been successfully anchored on the surface of the hollow mesoporous silica sub-microspheres.

The photoluminescence (PL) technique can reflect the recombination rate of the photoinduced electrons and holes, which are conducive to evaluate the photocatalytic performance of the semiconductor materials. Fig. 5 shows the PL spectrum of 5 wt.% HBPP and HBP synthesized at 140 °C. There are two lase wavelength for BiOCl at 360 nm and 420 nm corresponding to the two emission wavelength. It can be seen that one emission peak at around 539 nm is excited by 420 nm lase. Although the shapes and peaks positions of 5 wt.% HBPP are similar to HBP, the emission intensity decreases with the result of that weak recombination of the e⁻/h⁺ pairs to enhance photon efficiency.

N₂ adsorption-desorption isotherms and the corresponding BJH pore size distribution plots (inset) of the as-obtained H-mSiO₂ and HBPP composite were performed to determine the surface areas and pore size distributions of the composites, which can further explore the possibility of interconnected pores in the hollow mesoporous sphere photocatalyst. The BET surface area and the single-point total pore volume for H-mSiO₂ sub-microspheres came out to be 931.10 m²/g and 0.94 cm³/g, and that of 5 wt.% HBPP composite (obtained in 140 °C hydrothermal reaction) are 51.72 m²/g and 0.18 m³/g, respectively.

As Fig. 6a and b shows, the adsorption-desorption isotherms of H-mSiO₂ and HBPP composites identified as type IV indicating the pore structure of mesoporous. Moreover, the shape of hysteresis loop from Fig. 6a is of type H1, ascribing to open ends of cylindrical hole with the same diameter, which is in agreement with the structure of H-mSiO₂; and the shape of hysteresis loop from Fig. 6b is of type H3, which ascribes to the sheet-like structure being in agreement with the result as observed in Fig. 2b. In addition, as showed in the inset of Fig. 6a and b, the average BJH pore diameters of H-mSiO₂ and HBPP are 3 nm and approximately 30 nm, respectively. It is obvious that the BET surface area and pore volume of HBPP decrease, which can be attributed to the introduction of the BiOCl@PANI@Pd composites on the surface of the H-mSiO₂ sub-microspheres. Besides, the morphology change of the H-mSiO₂ sub-microspheres under high temperatures and pressures is also an important reason for the decreased BET surface area. In consequence, the large BET surface area and porous hollow structure

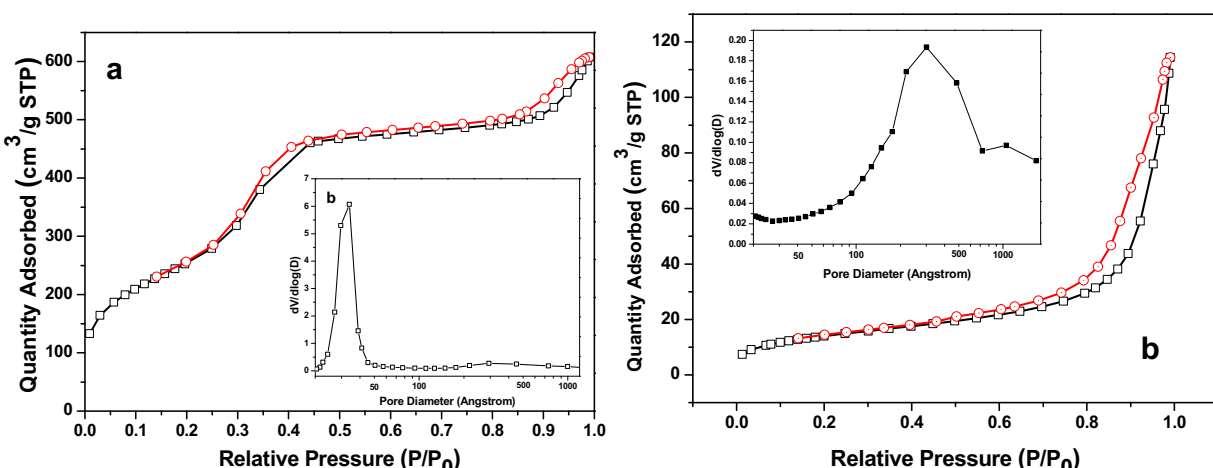


Fig. 6. N₂ adsorption/desorption isotherms and diameter distribution (in the corresponding figure) of (a) H-mSiO₂; (b) 5 wt.% HBPP synthesized hydrothermally in 140 °C.

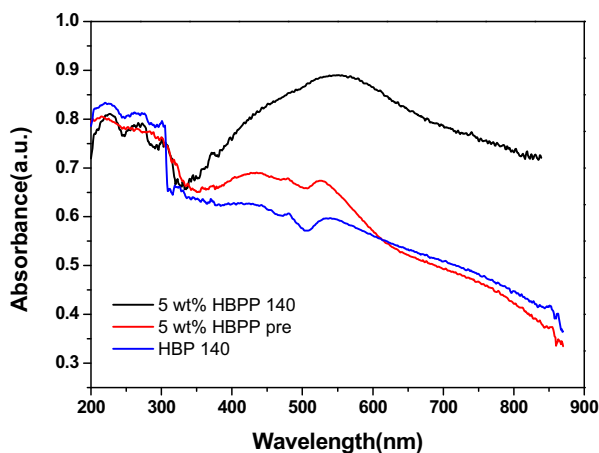


Fig. 7. UV-vis absorption spectra of as-prepared HBPP composites.

could facilitate more efficient contact of HBPP with organic contaminants, and may improve its photocatalytic activity to some extent.

For a VLD semiconductor photocatalyst, the optical absorption property is the key factor to determine its photocatalytic activity. Fig. 7 shows UV-vis absorption spectra of 5 wt.% HBPP composites before hydrothermal process, 5 wt.% HBPP composites and HBP composites synthesized at 140 °C. For the HBP composites, there are no significant absorption at wavelength longer than 400 nm, which is the intrinsic bandgap absorption of the BiOCl. After a certain amount of Pd was introduced, the light absorption strengthened in the visible light regions when compared to HBP composites. Nevertheless, a peak indicating the presence of a LSPR for the HBPP without hydrothermal is not observable. It is presumed that the Pd nanoparticles are not formed before hydrothermal process. While HBPP composites are prepared after hydrothermal process at 140 °C, it is nearly up to full spectrum absorption for visible light and a LSPR resonance peak can be observed at 545 nm. The strong interaction of Pd composites with electromagnetic fields also causes LSPR in the near-UV region, which is demonstrated to boost the excitation of electron-hole pairs in BiOCl and thereby increase photocatalytic efficiency.

3.2. Photocatalytic properties of the samples

MO, a major absorption band at 464 nm, was chosen as a representative dye to evaluate the photocatalytic activity of HBPP composite at different situation under visible light

($420 \text{ nm} < \lambda < 800 \text{ nm}$) irradiation. Herein, P25, commercially available photocatalyst, was also chosen as the contrast photocatalyst to decompose MO under visible light. By contrast, it was demonstrated that MO solution is hardly degraded without any catalyst under visible light irradiation.

To begin with, the adsorption of MO on the HBPP photocatalysts in the dark needed to be checked. It reveals that the removal efficiency of 20 mg/L and 50 mg/L MO is 94% and 68% after 30 min of the hollow mesoporous structure in the HBPP composite, which is 31 and 23 times than that of P25. Furthermore, HBPP composite has a miraculous effect on the dye of low concentration and could deal with the urgency environmental problems. Moreover, MO of high concentration hardly remains by the decomposition of optical HBPP composites under visible light in 230 min.

Fig. 8a shows photocatalytic degradation activity of MO (50 mg/L) over the 5 wt.% HBPP prepared at different temperature. It is known that the electric conductivity of PANI doped HCl varies with the hydrothermal temperature. The doping HCl would break away from the chain of PANI so that the photocatalytic efficiency degrades. In Fig. 8a, it is obvious that the hydrothermal temperature has an apparent effect on the photodgradation date. The removal dates are 84%, 97%, 89% and 88% while the samples are treated at 120 °C, 140 °C, 160 °C and 180 °C, respectively, which are much larger than that of P25. As hydrothermal temperature increases to 140 °C, the degradation date of HBPP composites has a steady and sustained increase, which has a good consistent with the characterization of XRD. After 140 °C, the degradation date of MO continuously decreases, and it agrees with previous studies.

The photodegradation efficiencies of MO (50 mg/L) mediated by HBPP photocatalysts with different weight percent of Pd under visible-light irradiation ($>420 \text{ nm}$) with identical conditions are displayed in Fig. 9a. In the photodegradation process, few MO can be photodegraded by HBP under visible light in 230 min. However, all HBPP photocatalysts exhibit higher photocatalytic activity than that of HBP. For another, the photocatalytic activity of the HBPP enhances with the Pd content until its optimum and declined further increase of Pd content. Due to Pd nanoparticles (NPs) attached to the BiOCl showing photoexcitation of localized surface plasmon resonance (LSPR), photocatalytic activity increases before the optimum. For further investigating the effect of Pd doping without any other factor, photocatalytic degradation activity of MO (50 mg/L) over pure BiOCl and BiOCl/Pd composites are carried out under visible light (Fig. 10), it is obviously observed that the photocatalytic degradation rate over BiOCl/Pd is 6.7 times than that of pure BiOCl. In addition, there is a sudden drop in primary stage of decomposition MO and the concentration of MO is almost invariant later,

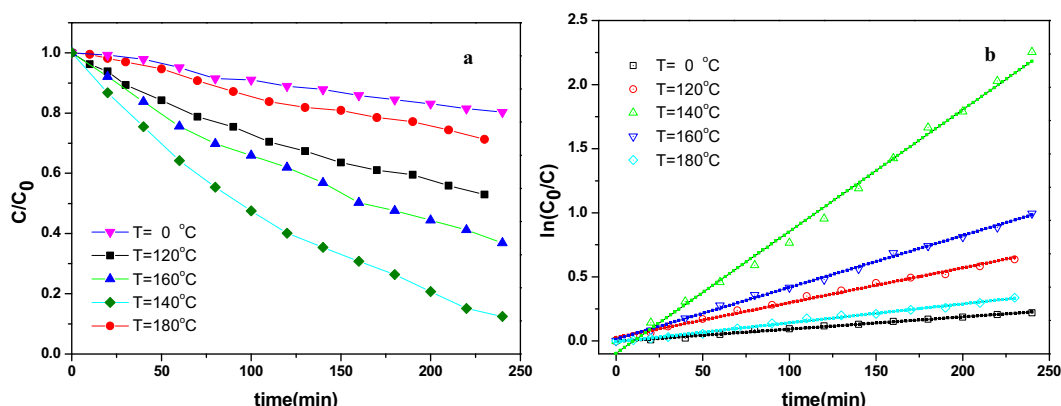


Fig. 8. Photocatalytic degradation activity (a) and the fitted kinetic plots of photocatalytic degradation processes (b) of MO under visible-light ($>420 \text{ nm}$) irradiation over the HBPP_{5wt.%} photocatalysts synthesized in different temperature.

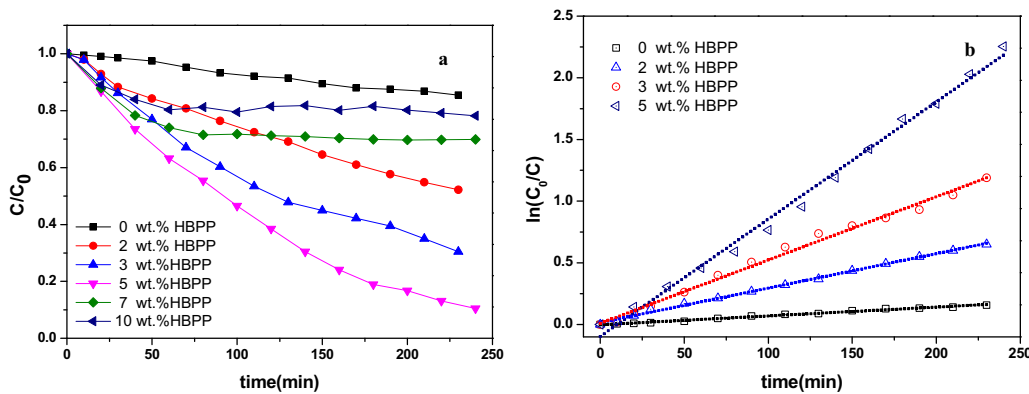


Fig. 9. Photocatalytic degradation activity (a) and the fitted kinetic plots of photocatalytic degradation processes (b) of MO under visible-light (>420 nm) irradiation over HBPP with different content of Pd synthesized in 140 $^{\circ}$ C.

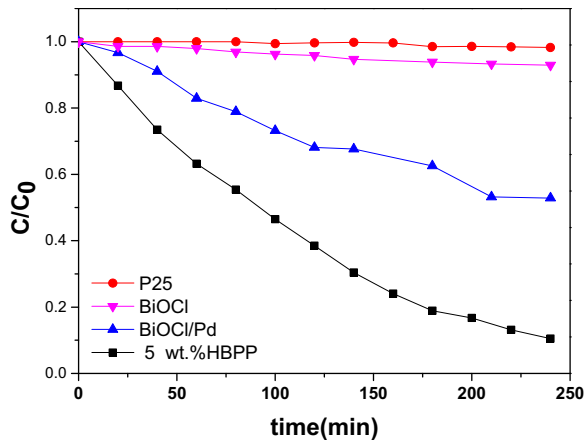


Fig. 10. Photocatalytic degradation activity of MO under visible-light (>420 nm) irradiation over P25, Pure BiOCl, BiOCl/Pd and 5 wt.% HBPP synthesized in 140 $^{\circ}$ C.

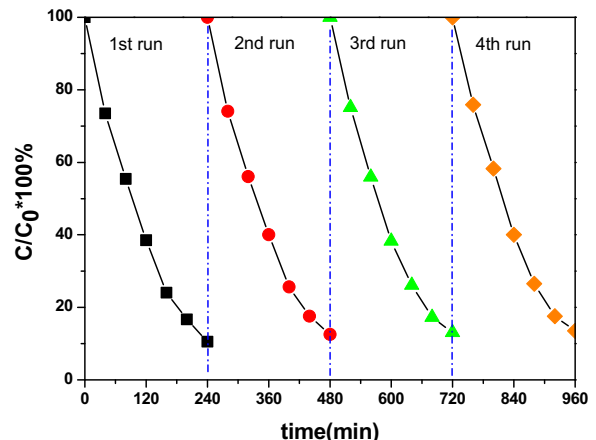


Fig. 11. Photodegradation of MO over HBPP photocatalyst during repeated operation under visible light irradiation.

which is due to the weak effect of LSPR by the aggregation of Pd nanoparticles with the sequentially increasing concentration of Pd.

To characterize the photocatalytic efficiency directly, the L-H kinetic model was introduced to analyze the process of decomposition. The photocatalytic degradation reaction can be assumed to follow a pseudo-first-order expression:

$$\ln(C_0/C) = k_{app} \cdot t$$

Where \$k_{app}\$ is the apparent rate constant (\$\text{min}^{-1}\$), C is the solution phase concentration of MB, \$C_0\$ is the initial concentration at \$t=0\$.

The variations in \$\ln(C_0/C)\$ as a function of illumination time are given in Figs. 8b and 9b. It is found that the 5 wt.% HBPP (synthesized in 140 $^{\circ}$ C) exhibits the highest degradation rate (\$k=9.5 \cdot 10^{-3} \text{ min}^{-1}\$), which is 13.3 times of that over HBP, and this is coincident with Result of fluorescence detection.

To investigate the stability of the photocatalyst, the recycled experiments for the photodegradation of MO under visible light were carried out. As shown in Fig. 11, the 5 wt.% HBPP composite was directly used for the photocatalyst without any treatment in every recycle. And the removal rate of the second and the third experiment are 97% and 98%, respectively. Moreover, it is almost a constant value after several recycles, which implies the HBPP is relatively stable during the photocatalytic degradation process, and thus the HBPP has a promising application in industry.

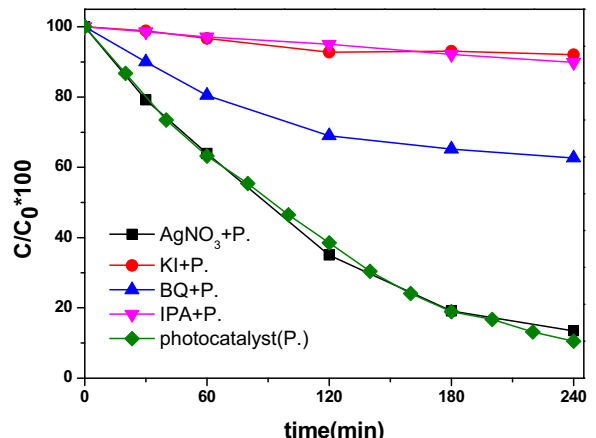
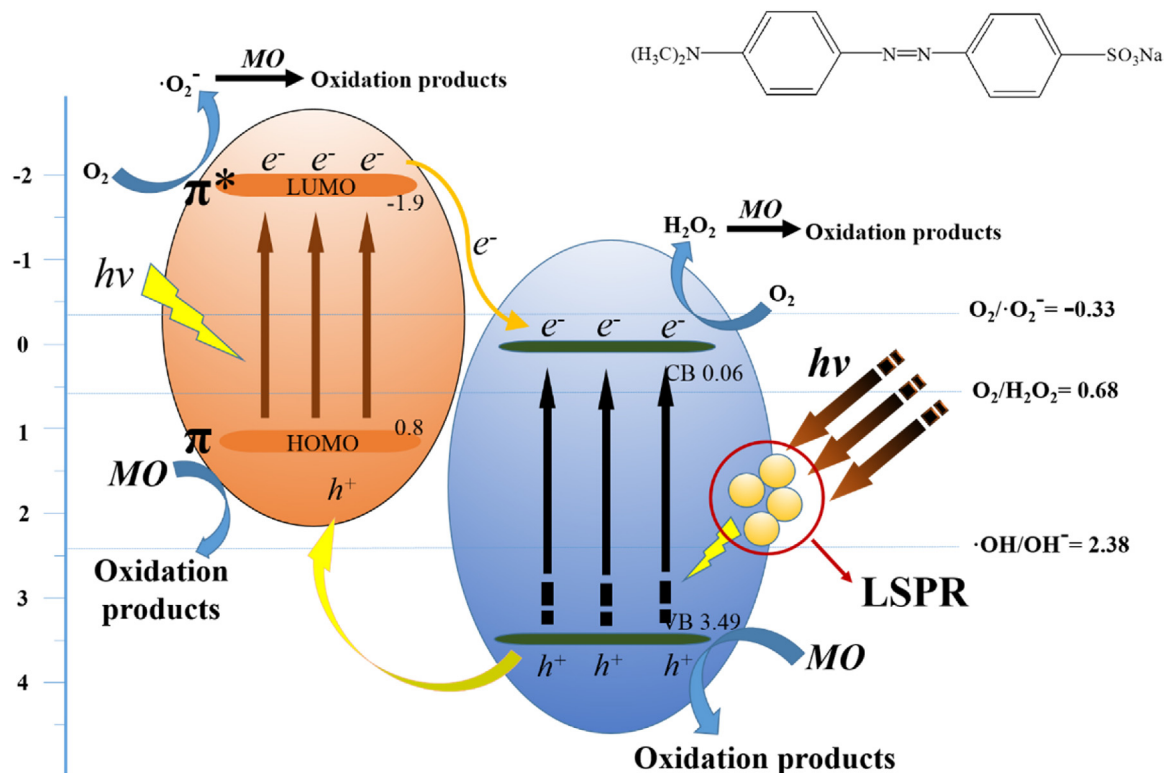


Fig. 12. Photocatalytic degradation of MO over HBPP under different conditions with exposure to the visible light.

3.3. Discussion of photocatalytic mechanism

In order to identify the involvement of active radical species in the photocatalytic process, the controlled experiments with different types of active species scavengers added in catalyst system are carried out. It is well known that holes (\$h^+\$), super oxygen free radicals (\$\bullet O_2^-)\$, and hydroxyl radicals (\$\bullet OH)\$ and \$e^-)\$ are the main



Scheme 1. Proposed mechanism for the visible light photodegradation of MO over HBPP composites.

reactive species and trigger the oxidation of organic pollutants (Fig. 12).

When KI (2 mg) as a scavenger for holes is added in the system, the degradation rate of MO decreases remarkably, from which we can conclude the dominate role of hole in the process of photocatalytic degradation. The benzoquinone, which has the ability to trap $\cdot O_2^-$ by a simple electron transfer mechanism, has a partial inhibition of the MO degradation. In addition, IPA as a scavenger for $\cdot OH$ added, the rate for degradation of MO decreases sharply, which indicates the important role of $\cdot OH$ in the reaction. Moreover, as an e^- scavenger, $AgNO_3$ was added to the reaction system, thus the photodegradation activity only had a slight decrease. Based the comparison above, it is concluded that the MO oxidation is mainly driven by the participation of hole and $\cdot OH$ radicals and to a lesser extent by the contribution of $\cdot O_2^-$ radicals.

The electron paramagnetic resonance (EPR) with 5,5-dimethyl-1-pyrroline-N-oxide (DMPO) technique (EPR/DMPO) was performed to detect the active species generated by the 5 wt.% HBPP synthesized at 140 °C under visible light. Firstly, it was carried out in a methanol solution to detect whether there were any superoxide radicals ($\cdot O_2^-$) generated during the reaction process. As shown in Fig. 13a no EPR signal exists before irradiation. And after that, six weak peaks with relatively similar height are observed, which is corresponding to the characteristic signal peaks of the DMPO- $\cdot O_2^-$ adducts. Furthermore, additional experiments were performed in a water solution to detect whether any hydroxyl ($\cdot OH$) were generated during the reaction process. Before irradiation, there is identically no EPR signal (Fig. 13b). And after that, a quartet of signals with relative intensities of 1:2:2:1 from the DMPO- $\cdot OH$ adducts are detected, indicating that hydroxyl radicals are really formed in the catalytic reaction. Furthermore, it is obvious that the EPR signal intensity of DMPO- $\cdot OH$ adducts is much stronger than that of DMPO- $\cdot O_2^-$ adducts, which coincides with the conclusions on the controlled experiments.

We have discussed in detail the optical properties and the excellent photocatalytic property of HBPP, as well as the roles of the active radical species taking part in the process of the photocatalytic degradation. Based on all the above results and discussion, we can depict a probable mechanism with LSPR of Pd nanoparticles and the synergistic effect between PANI and BiOCl. It has reported that the various types of dyes have different molecular structures, which results in different degradation mechanisms. And the dye will degrade to carbon dioxide or other inorganic products (i.e. SO_4^{2-} , N_2 , NO_3^-) by the active species over the photocatalyst attached by irradiation. In this study, azo-dye MO, which contains N=N double bond and the sulfonyl group located on the *p*-benzene ring, is preferable to evaluate the photocatalytic properties. In this process, the intermediates are presumably formed by the attack of oxidative species, and it contains two primary processes- demethylation and hydroxylation. For azo-dye MO, the central azo-group (N=N) is converted into gaseous dinitrogen (N_2), and the sulfonyl group is converted into innocuous SO_4^{2-} ions and the aromatic rings turn into CO_2 . The proposed degradation mechanism of MO over HBPP and the relationship of band structure between PANI and BiOCl are schematically presented in Scheme 1.

On the other hand, to explain the enhanced photocatalytic activity mechanism, conduction band minimum (CBM) and valence band maximum (VBM) potentials of PANI and BiOCl should be confirmed. We know that the highest occupied molecular orbital (HOMO) and the lowest unoccupied molecular orbital (LUMO) of PANI are 0.8 eV and -1.9 eV [26], which can absorb visible light to induce $\pi-\pi^*$ transition, delivering the excited-state electrons from HOMO orbital to LUMO orbital. Nevertheless the valence band and conduction band potentials of BiOCl are 3.49 eV and 0.06 eV [19], respectively, which indicates that BiOCl can not be excited under visible light irradiation and only absorb UV light irradiation. Moreover, Pd NPs show a very intense LSPR absorption band in the near-UV region. Therefore, we hypothesized that this enhanced near-field could boost the excitation of electron-hole pairs in BiOCl

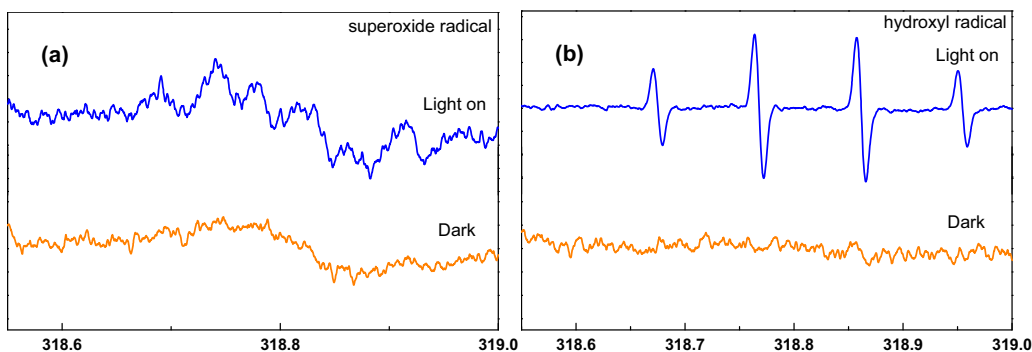


Fig. 13. EPR spectra of DMPO trapped (a) $\bullet\text{O}_2^-$ in methanol and (b) $\bullet\text{OH}$ in water with the photocatalyst of 5 wt.% HBPP synthesized at 140 °C under visible light irradiation.

and increase the efficiency of the photocatalysis. The HOMO and LUMO of PANI match well with the energy band of BiOCl and have chemical bond interaction, which is contributed to cause synergistic effect[30]. When irradiated by appropriate light, electrons are excited from the HOMO to the LUMO of PANI, which could produce $\bullet\text{O}_2^-$. As the lowest unoccupied molecular orbital (LUMO) level of PANI is more negative than the conduction band (CB) of BiOCl, the electrons partly inject into the CBM of BiOCl and subsequently transfer to the surface to react with water and oxygen to yield hydroxyl, which would oxidize the MO. Meanwhile, the photogenerated holes transfer from the CB of BiOCl toward the LUMO of the PANI, and attach the MO. Depended on the interacting interface between the BiOCl and PANI, the transference process of electron and hole makes a rapid photogenerated charge separation and inhibits the pairs of electron-hole recombination, which significantly enhances the photocatalytic property of the HBPP photocatalysts. Moreover, as the carrier of photocatalyst, the orderly mesoporous opening structure of the hollow mesoporous SiO_2 sphere could effectively facilitate the transfer of reactant molecules, and the existence of the internal cavities would effectively prolong the action time of the irradiated light for the multiple reflections. In consequence, it would lead to the enhanced photocatalytic property of the BiOCl@PANI@Pd nanophotocatalyst on the surface of the H-mSiO₂ sub-microspheres.

4. Conclusion

In summary, a special H-mSiO₂-BiOCl@PANI@Pd (HBPP) photocatalyst has been successfully synthesized by a facile method. The excellent photocatalytic properties of the HBPP are investigated by the photocatalytic degradation of MO under the visible light. It is determined that the hole and $\bullet\text{OH}$ play extremely important role in the photocatalytic reaction. And the photocatalytic activity of this novel HBPP composite is superior to that of HBP composite, and shows excellent photocatalytic properties under visible-light irradiation. This is largely due to their unique structure and performance such as the orderly mesoporous opening structure, the internal cavities, the fast migration of the interface charges, and SPR absorption band in the near-UV region.

Acknowledgement

The authors are grateful for the financial support provided by the State Key Program of National Natural Science of China (Grant No. 51433008), the National Natural Science Foundation of China (Grant No. 51673156) and the Natural Science Foundation of Shaanxi Province (Grant No.2015JQ2055).

Appendix A. Supplementary data

Supplementary data associated with this article can be found, in the online version, at <http://dx.doi.org/10.1016/j.apcatb.2017.05.026>.

References

- [1] X. Chen, S. Shen, L. Guo, S.S. Mao, Semiconductor-based photocatalytic hydrogen generation, *Chem. Rev.* 110 (2010) 6503–6570.
- [2] N. Guo, Y. Liang, S. Lan, L. Liu, J. Zhang, G. Ji, S. Gan, Microscale hierarchical three-dimensional flowerlike TiO_2 /PANI composite: synthesis, characterization, and its remarkable photocatalytic activity on organic dyes under UV-light and sunlight irradiation, *J. Phys. Chem. C* 118 (2014) 18343–18355.
- [3] J. Jiang, L. Zhang, H. Li, W. He, J.J. Yin, Self-doping and surface plasmon modification induced visible light photocatalysis of BiOCl, *Nanoscale* 5 (2013) 10573–10581.
- [4] B. Zhang, P. Li, H. Zhang, H. Wang, X. Li, L. Tian, N. Ali, Z. Ali, Q. Zhang, Preparation of lipase/ $\text{Zn}_3(\text{PO}_4)_2$ hybrid nanoflower and its catalytic performance as an immobilized enzyme, *Chem. Eng. J.* 291 (2016) 287–297.
- [5] B. Zhang, J. Wang, J. Chen, H. Li, H. Wang, H. Zhang, $\text{Fe}_3\text{O}_4@\text{P}(\text{DVB}/\text{MAA})/\text{Pd}$ composite microspheres: preparation and catalytic degradation performance, *RSC Adv.* 6 (2016) 100598–100604.
- [6] S. Zhan, D. Chen, X. Jiao, C. Tao, Long TiO_2 hollow fibers with mesoporous walls: sol-gel combined electrospun fabrication and photocatalytic properties, *J. Phys. Chem. B* 110 (2006) 11199–11204.
- [7] Q. Dong, S. Yin, C. Guo, X. Wu, N. Kumada, T. Takei, A. Miura, Y. Yonesaki, T. Sato, Single-crystalline porous NiO nanosheets prepared from $\beta\text{-Ni(OH)}_2$ nanosheets: magnetic property and photocatalytic activity, *Appl. Catal. B-Environ.* 147 (2014) 741–747.
- [8] T.K. Townsend, N.D. Browning, F.E. Osterloh, Overall photocatalytic water splitting with $\text{NiO}_x\text{-SrTiO}_3$ —a revised mechanism, *Energ. Environ. Sci.* 5 (2012) 9543–9550.
- [9] Y. Zhang, N. Zhang, Z.-R. Tang, Y.-J. Xu, Graphene transforms wide band gap ZnS to a visible light photocatalyst. The new role of graphene as a macromolecular photosensitizer, *ACS Nano* 6 (2012) 9777–9789.
- [10] M. Liu, F. Li, Z. Sun, L. Xu, Y. Song, A. Munventwali, Enhanced photocatalytic H_2 evolution on CdS with cobalt polyoxotungstosilic acid and MoS_2 /graphene as noble-metal-free dual co-catalysts, *RSC Adv.* 5 (2015) 47314–47318.
- [11] H. Cheng, B. Huang, P. Wang, Z. Wang, Z. Lou, J. Wang, X. Qin, X. Zhang, Y. Dai, In situ ion exchange synthesis of the novel Ag/AgBr/BiOBr hybrid with highly efficient decontamination of pollutants, *Chem. Commun.* 47 (2011) 7054–7056.
- [12] P. Wang, T. Ming, G. Wang, X. Wang, H. Yu, J. Yu, Cocatalyst modification and nanonization of Ag/AgCl photocatalyst with enhanced photocatalytic performance, *J. Mol. Catal. A-Chem.* 381 (2014) 114–119.
- [13] M. Zhu, P. Chen, M. Liu, Graphene oxide enwrapped Ag/AgX (X = Br, Cl) nanocomposites as a highly efficient visible-light plasmonic photocatalyst, *Acad. Nano* 5 (2011) 4529–4536.
- [14] J. Jiang, K. Zhao, X. Xiao, L. Zhang, Synthesis and facet-dependent photoreactivity of BiOCl single-crystalline nanosheets, *J. Am. Chem. Soc.* 134 (2012) 4473–4476.
- [15] D. Zhang, J. Li, Q. Wang, Q. Wu, High {001} facets dominated BiOBr lamellas: facile hydrolysis preparation and selective visible-light photocatalytic activity, *J. Mater. Chem. A* 1 (2013) 8622–8629.
- [16] Y. Wang, K. Deng, L. Zhang, Visible light photocatalysis of BiOI and its photocatalytic activity enhancement by in situ ionic liquid modification, *J. Phys. Chem. C* 115 (2011) 14300–14308.
- [17] X. Zhang, Z. Ai, F. Jia, L. Zhang, Generalized one-pot synthesis characterization, and photocatalytic activity of hierarchical BiOX (X = Cl, Br, I) nanoplate microspheres, *J. Phys. Chem. C* 112 (2008) 747–753.

- [18] A.K. Chakraborty, S.B. Rawal, S.Y. Han, S.Y. Chai, W.I. Lee, Enhancement of visible-light photocatalytic efficiency of BiOCl/Bi₂O₃ by surface modification with WO₃, *Appl. Catal. A-Gen.* 407 (2011) 217–223.
- [19] J. Di, J. Xia, M. Ji, B. Wang, S. Yin, Q. Zhang, Z. Chen, H. Li, Carbon quantum dots modified BiOCl ultrathin nanosheets with enhanced molecular oxygen activation ability for broad spectrum photocatalytic properties and mechanism insight, *ACS Appl. Mater. Interface* 7 (2015) 20111–20123.
- [20] C. Huang, J. Hu, S. Cong, Z. Zhao, X. Qiu, Hierarchical BiOCl microflowers with improved visible-light-driven photocatalytic activity by Fe (III) modification, *Appl. Catal. B-Environ.* 174 (2015) 105–112.
- [21] L. Yu, X. Zhang, G. Li, Y. Cao, S. Yu, D. Li, Highly efficient Bi₂O₂CO₃/BiOCl photocatalyst based on heterojunction with enhanced dye-sensitization under visible light, *Appl. Catal. B-Environ.* 187 (2016) 301–309.
- [22] S. Ghosh, N.A. Kouamé, L. Ramos, S. Remita, A. Dazzi, A. Deniset-Besseau, P. Beaunier, F. Goubard, P.-H. Aubert, H. Remita, Conducting polymer nanostructures for photocatalysis under visible light, *Nat. Mater.* 14 (2015) 505–511.
- [23] J. Li, L. Zhu, Y. Wu, Y. Harima, A. Zhang, H. Tang, Hybrid composites of conductive polyaniline and nanocrystalline titanium oxide prepared via self-assembling and graft polymerization, *Polymer* 47 (2006) 7361–7367.
- [24] S. Cao, J. Yu, g-C₃N₄-based photocatalysts for hydrogen generation, *J. Phys. Chem. Lett.* 5 (2014) 2101–2107.
- [25] Y. Sui, J. Liu, Y. Zhang, X. Tian, W. Chen, Dispersed conductive polymer nanoparticles on graphitic carbon nitride for enhanced solar-driven hydrogen evolution from pure water, *Nanoscale* 5 (2013) 9150–9155.
- [26] L. Ge, C. Han, J. Liu, In situ synthesis and enhanced visible light photocatalytic activities of novel PANI–gc 3 N 4 composite photocatalysts, *J. Mater. Chem.* 22 (2012) 11843–11850.
- [27] M.O. Ansari, M.M. Khan, S.A. Ansari, J. Lee, M.H. Cho, Enhanced thermoelectric behaviour and visible light activity of Ag@TiO₂/polyaniline nanocomposite synthesized by biogenic-chemical route, *RSC Adv.* 4 (2014) 23713–23719.
- [28] M. Radoičić, Z. Šaponjić, I. Janković, G. Čirić-Marjanović, S. Ahrenkiel, M. Čomor, Improvements to the photocatalytic efficiency of polyaniline modified TiO₂ nanoparticles, *Appl. Catal. B-Environ.* 136 (2013) 133–139.
- [29] H. Zhang, R. Zong, J. Zhao, Y. Zhu, Dramatic visible photocatalytic degradation performances due to synergistic effect of TiO₂ with PANI, *Environ. Sci. Technol.* 42 (2008) 3803–3807.
- [30] Z. Pei, L. Ding, M. Lu, Z. Fan, S. Weng, J. Hu, P. Liu, Synergistic effect in polyaniline-hybrid defective ZnO with enhanced photocatalytic activity and stability, *J. Phys. Chem. C* 118 (2014) 9570–9577.
- [31] K. Awazu, M. Fujimaki, C. Rockstuhl, J. Tominaga, H. Murakami, Y. Ohki, N. Yoshida, T. Watanabe, A plasmonic photocatalyst consisting of silver nanoparticles embedded in titanium dioxide, *J. Am. Chem. Soc.* 130 (2008) 1676–1680.
- [32] X. Yan, X. Zhu, R. Li, W. Chen, Au/BiOCl heterojunction within mesoporous silica shell as stable plasmonic photocatalyst for efficient organic pollutants decomposition under visible light, *J. Hazard. Mater.* 303 (2016) 1–9.
- [33] J. Yu, G. Dai, B. Huang, Fabrication and characterization of visible-light-driven plasmonic photocatalyst Ag/AgCl/TiO₂ nanotube arrays, *J. Phys. Chem. C* 113 (2009) 16394–16401.
- [34] L. Zhou, C. Zhang, M. McClain, A. Manjavacas, C.M. Krauter, S. Tian, F. Berg, H.O. Everitt, E.A. Carter, P. Nordlander, Aluminum nanocrystals as a plasmonic photocatalyst for hydrogen dissociation, *Nano Lett.* (2016).
- [35] A. Tittl, P. Mai, R. Taubert, D. Dregely, N. Liu, H. Giessen, Palladium-based plasmonic perfect absorber in the visible wavelength range and its application to hydrogen sensing, *Nano Lett.* 11 (2011) 4366–4369.
- [36] E. Kowalska, K. Yoshihri, Z. Wei, S. Zheng, E. Kastl, H. Remita, B. Ohtani, S. Rau, Hybrid photocatalysts composed of titania modified with plasmonic nanoparticles and ruthenium complexes for decomposition of organic compounds, *Appl. Catal. B-Environ.* 178 (2015) 133–143.
- [37] E.J. Crossland, N. Noel, V. Sivaram, T. Leijtens, J.A. Alexander-Webber, H.J. Snaith, Mesoporous TiO₂ single crystals delivering enhanced mobility and optoelectronic device performance, *Nature* 495 (2013) 215–219.
- [38] W. Li, X. Jia, P. Li, B. Zhang, H. Zhang, W. Geng, Q. Zhang, Hollow mesoporous SiO₂–BiOBr nanophotocatalyst: synthesis, characterization and application in photodegradation of organic dyes under visible-Light irradiation, *ACS Sustainable Chem. Eng.* 3 (2015) 1101–1110.
- [39] W. Li, D. Zhao, Extension of the stöber method to construct mesoporous SiO₂ and TiO₂ shells for uniform multifunctional core–shell structures, *Adv. Mater.* 25 (2013) 142–149.